Revised Figures

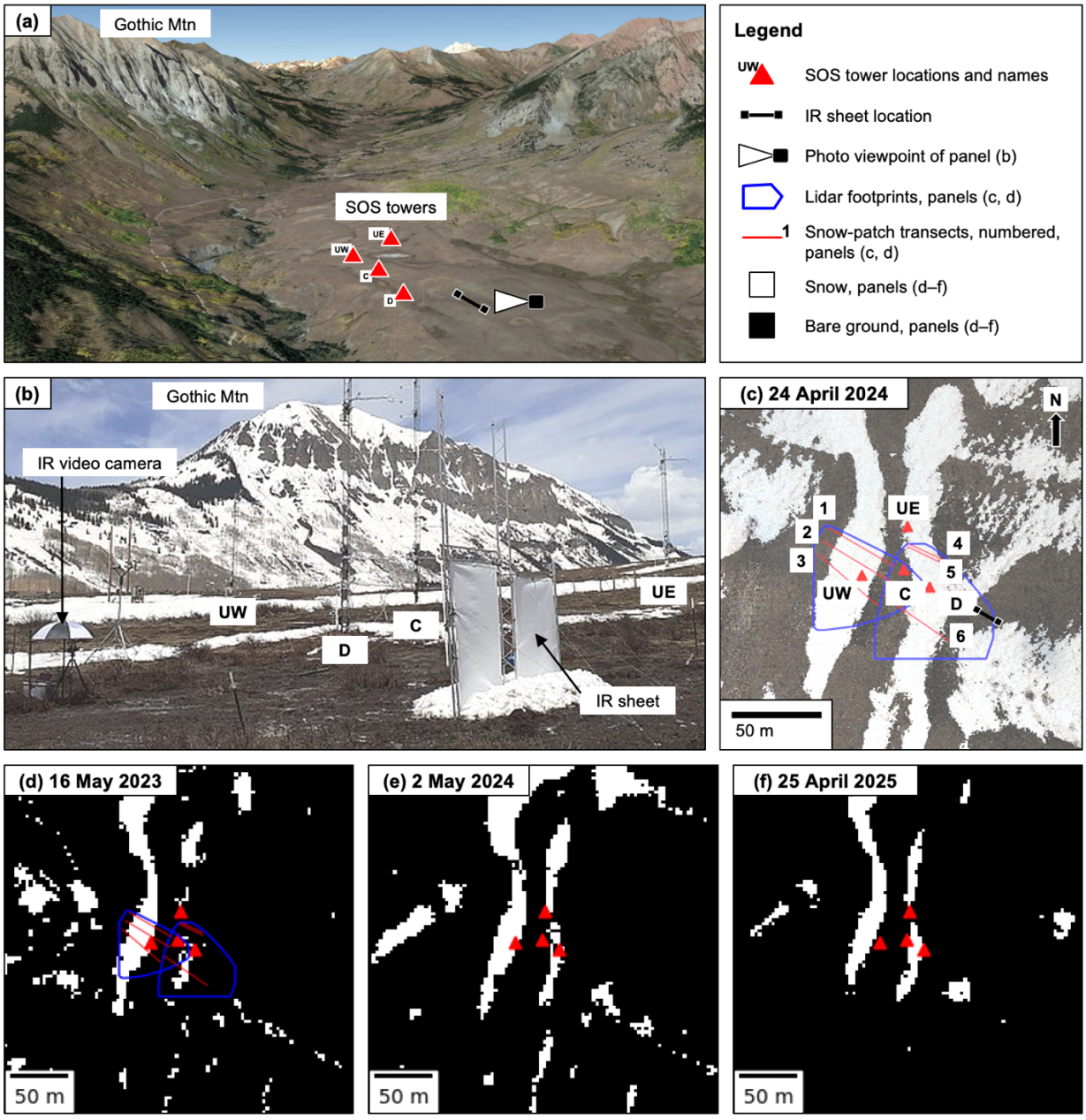


Figure 1. a) Oblique view of the upper East River Valley, looking upvalley (Source: Google Earth; Imagery ©2025 Airbus, Landsat, Copernicus). The approximate location of the Kettle Ponds site is shown with the relative location of the four towers, the IR sheet, and the approximate viewpoint of the photograph shown in panel b. Tower locations are not to scale. b) Photograph of the infrared (IR) video camera with umbrella, IR observation sheet, and the four instrument towers. c) Orthoimage of the Kettle Ponds site, collected by unmanned aerial vehicle, on 24 April 2024. Red triangles show true tower locations. Blue lines show footprints of scanning lidars mounted on towers UE and C. Red lines show six transects for which we extracted lidar measurements. d–f) Fractional snow covered area (fSCA) maps derived from 3-meter resolution Planet imagery (PBC, 2020/2025) using PlanetSCA software (Yang et al., 2023; Chiu et al., 2025). fSCA maps on days from three separate years were selected to illustrate the consistent location of snow patches during the melt season. Includes copyrighted material of Planet Labs PBC. All rights reserved.

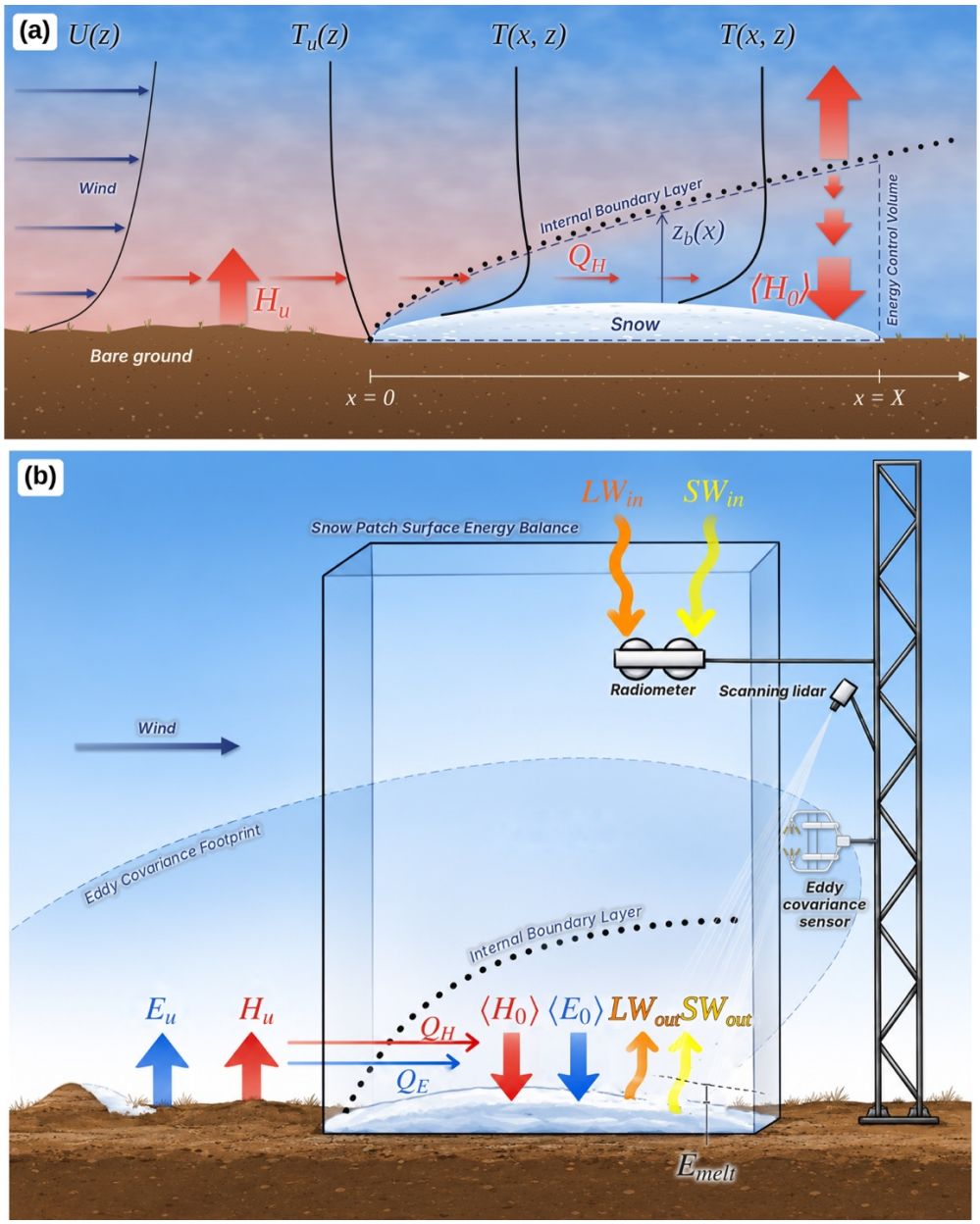


Figure 3. (a) Conceptual diagram illustrating the development of an internal boundary layer (IBL) over a snow patch. $U(z)$ is the horizontal wind speed profile, which is assumed to be constant across bare ground and snow. $T_u(z)$ is the temperature profile over bare ground and $T(x,z)$ is the temperature profile over the snow, which varies with distance into the snow patch. $z_b(x)$ is the depth of the flux IBL formed over the snow patch, defined as the height where the sensible heat flux above snow equals the sensible heat flux above bare ground. H_u is the upward sensible heat flux over the bare ground, Q_H is the horizontally advected sensible heat, and $\langle H_0 \rangle$ is the horizontally-averaged sensible heat flux into the snow patch. Advected sensible heat (Q_H) decreases with distance into the snow patch and this horizontal flux divergence is associated with a deposition of heat into the snow patch. The conservation of heat equation (Equation 1) is integrated over the Energy Control Volume in the atmosphere over the snow patch, which is defined between $z = 0$ and $z = z_b$ and between $x = 0$ and $x = X$. (b) Conceptual diagram illustrating our approach to measuring the energy balance over a snow patch. All instruments illustrated were deployed at the Kettle Ponds site. Transport terms for latent heat fluxes, equivalent to the sensible heat flux terms described in panel a, are included ($E_u, Q_E, \langle E_0 \rangle$). The Snow-Patch Surface Energy Balance box includes all the terms in the energy balance equation (Equations 6 and 7). $\langle H_0 \rangle$ and $\langle E_0 \rangle$ are functions of terms outside the box, $\langle H_0 \rangle = H_u + Q_H$ and $\langle E_0 \rangle = E_u + Q_E$.

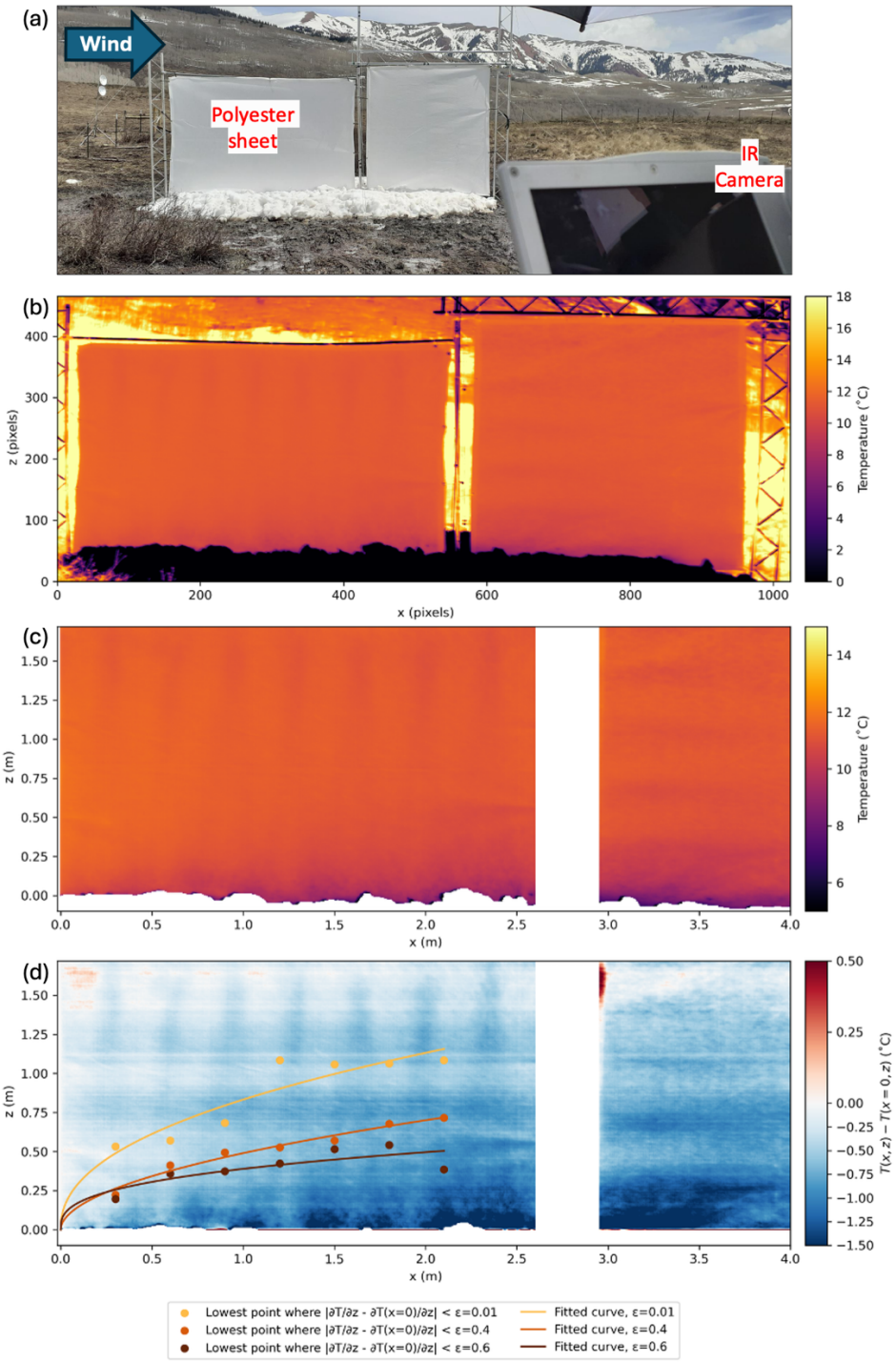


Figure 4. Illustration of the infrared video camera data collection method. a) Picture of the polyester observation sheet, from the vantage point of the infrared (IR) video camera. b) Mean measured temperature field, $T(x, z)$, observed by the IR video camera over 30 minutes, between 12:00–12:30 LT on 17 May 2023. Includes landscape behind the observation sheet. c) Same as panel b, but cropped to remove image pixels showing the landscape behind the observation sheet and the snow patch beneath. d) Temperature anomaly field, defined as the difference between the measured temperature field and the vertical profile of temperature at the left edge of the IR observation sheet, $T(x, z) - T(x = 0, z)$. Estimates of the internal boundary layer are included.

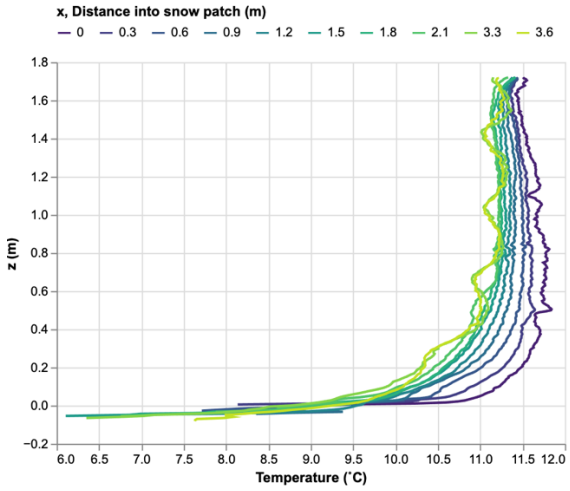


Figure 6. Vertical profiles of air temperature measured by the IR camera at different distances (x) into the snow patch. Each profile is a horizontal average over a section of the IR image, and line color shows distance from the upwind edge of the snow patch (x = 0 m).

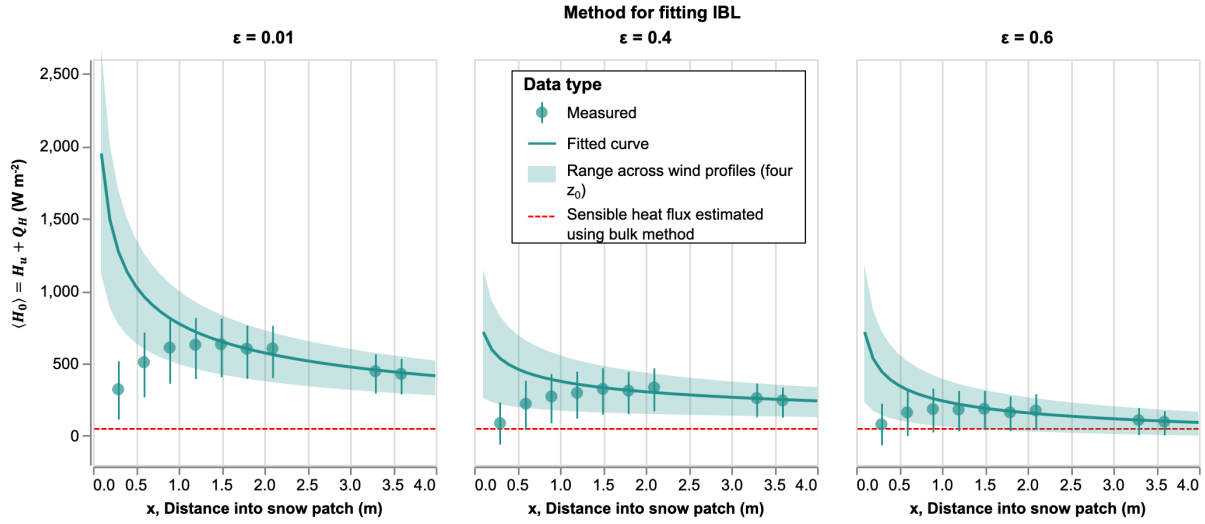


Figure 7. Patch-averaged sensible heat flux into snow, $\langle H_0 \rangle = H_u + Q_H$, as a function of distance into the snow patch, x. Panels show results for the three IBL height functions, $z_b(x)$, determined with ϵ = 0.01, 0.4 and 0.6 (Figure 4d). Measured values are calculated with Equation 2 from the mean temperature field collected over 30 minutes by the infrared video camera, using four logarithmic wind profiles based on the roughness lengths estimated at each of the four towers (z_0 = 0.004–0.065 m). Points show the mean measured $\langle H_0 \rangle$ across the four wind profiles, and vertical bars show the minimum and maximum. Fitted curves represent Equation 5 fitted to the measured data at $x > 1.2$ m using the least squares method; solid lines show the mean of the four fitted functions, and shading shows the range between the minimum and maximum. The dashed red line shows the sensible heat flux into the snow estimated with the bulk method [REFERENCE SECTION THAT ELABORATES ON THIS METHOD].

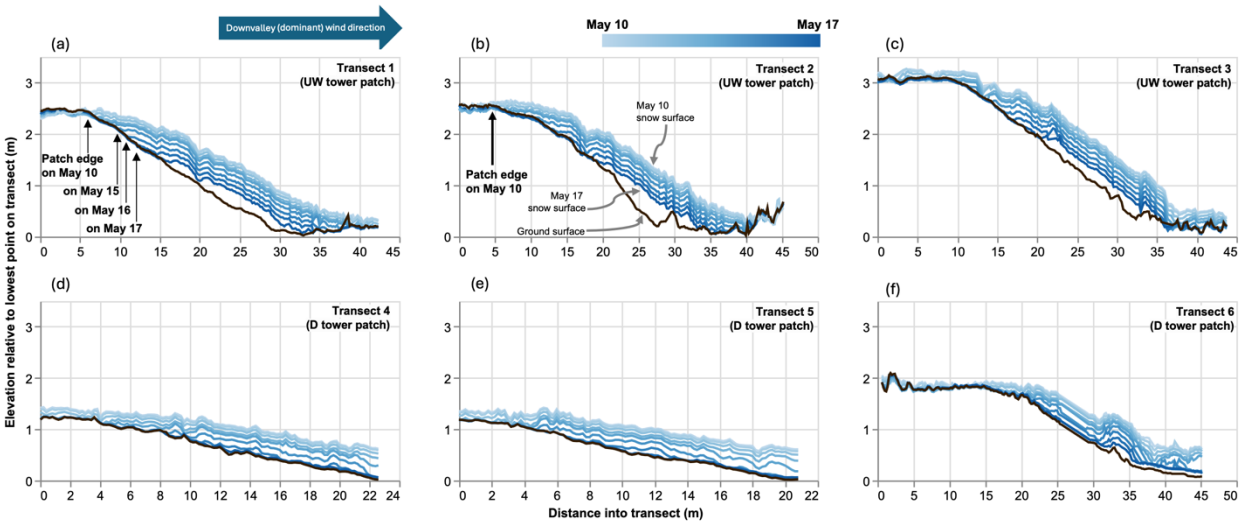


Figure 8. Surface elevations extracted over the six transects (Figure 1c) from lidar scans. One surface elevation transect is shown for each day between 10–17 May, from the scan collected at 00:00 LT. Blue lines show the changing snow surface. Black lines show the underlying ground surface. In panels a and b, black arrows point to the upwind edges of the snow patches, which evolve with time (illustrated in panel a). Aspects are vertically exaggerated.

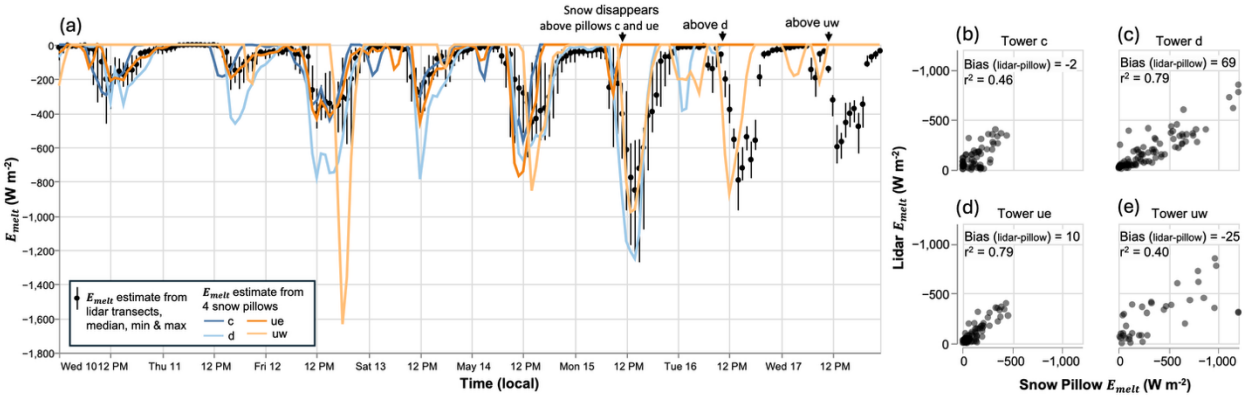


Figure 10. (a) Time series of E_{melt} estimated from lidar and from four snow pillows. Negative values indicate energy consumed by melt. Snow pillow and lidar change rates are calculated using second-order differencing. Lidar surface elevation change rates are converted to mass change rates using snow densities of 500, 550 and 600 kg m^{-3}. Black dots and bars show the median, minimum and maximum of lidar E_{melt} across all combinations of the six snow patches and three snow densities. Colored lines show E_{melt} estimated from the snow pillows at towers C, D, UE and UW. Arrows indicate when snow melted out above each snow pillow; after these times the pillows are visible in Figure 2. (b)–(e) Comparison of median lidar E_{melt} and snow pillow E_{melt} at towers C, D, UE and UW. Data from the 24 hours before snow melted out above each pillow are excluded, so the comparison includes data through 13 May for towers C and UE and through 15 May for towers D and UW. Each panel gives the mean bias (median lidar minus pillow, W m^{-2}) and the coefficient of determination (r^2) between median lidar and pillow E_{melt}.

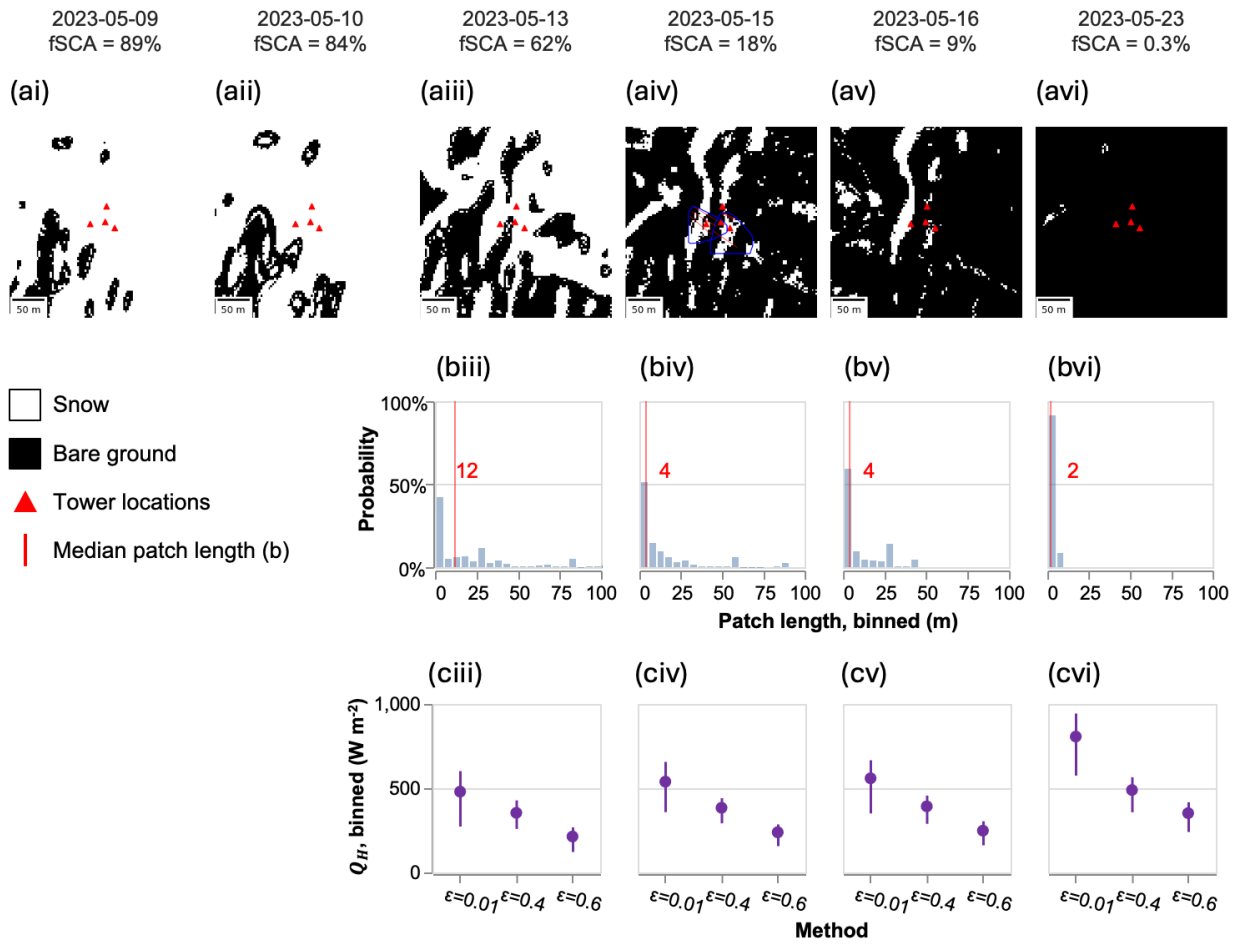


Figure 11. Snow cover, snow patch lengths and estimated sensible heat advection. (ai)–(avi) Fractional snow-covered area (fSCA) maps from six days in May 2023, overlapping with the study period. Red triangles show tower locations. Includes copyrighted material of Planet Labs PBC. All rights reserved. (biii)–(bvi) Distributions of snow patch lengths along the mean wind direction, calculated from the fSCA maps in panels (aiii)–(avi). The vertical red line and red text show the median patch length (m). Patch lengths are not shown for 9 and 10 May when fSCA > 62% and snow cover was too extensive for our advection model to apply (Section 3.5). (ciii)–(cvi) Sensible heat advection, Q_H, calculated with Equation 5 for each patch length in panels (biii)–(bvi), for each of the three IBL height functions (ϵ = 0.01, 0.4 and 0.6) and for all four wind profiles. Points show the mean Q_H across all snow patches and wind profiles, bars show the interquartile range.

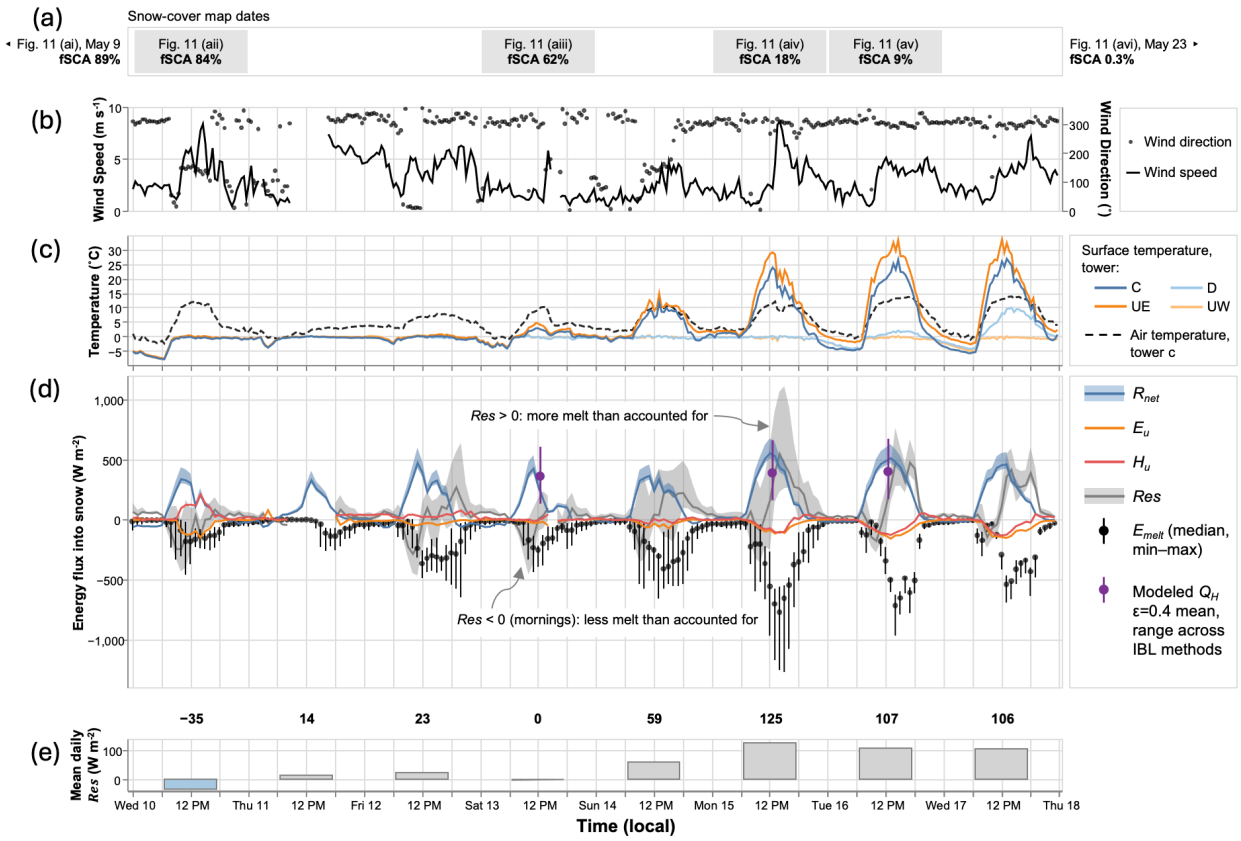
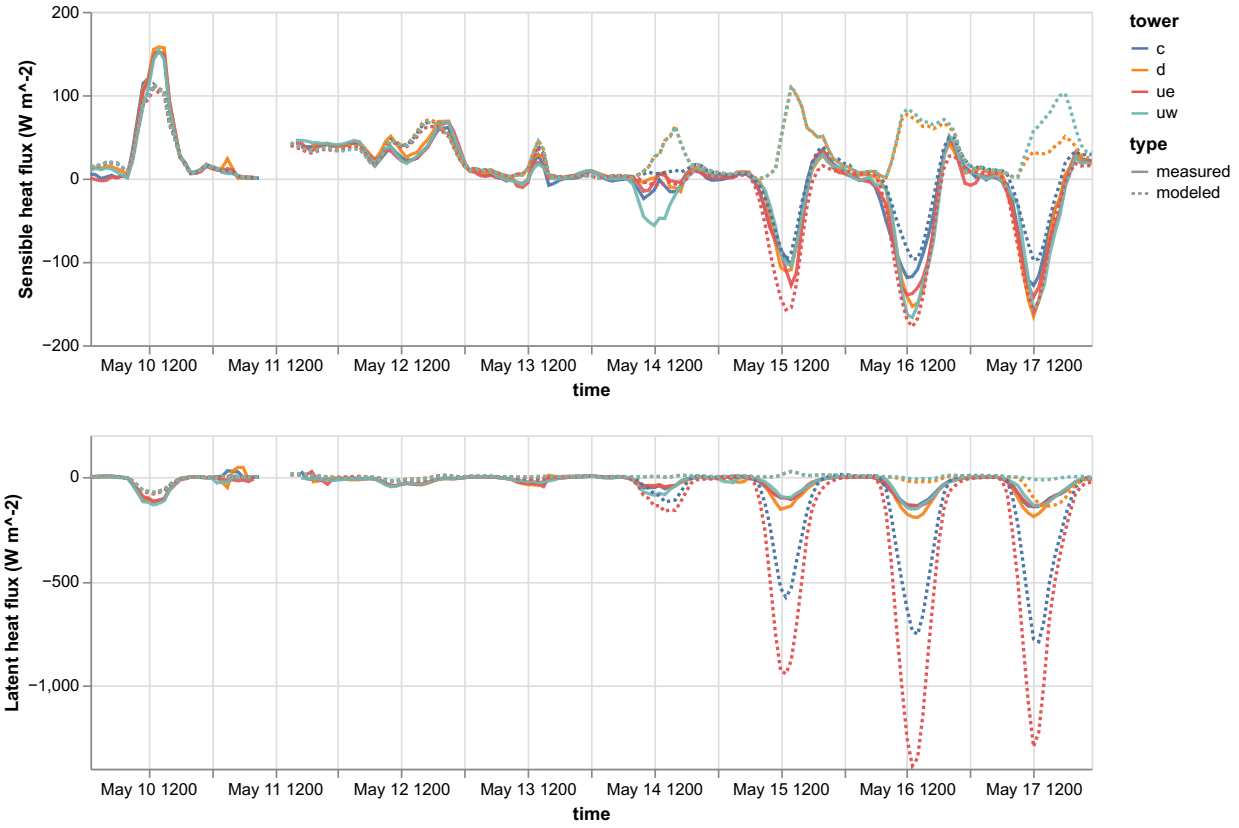
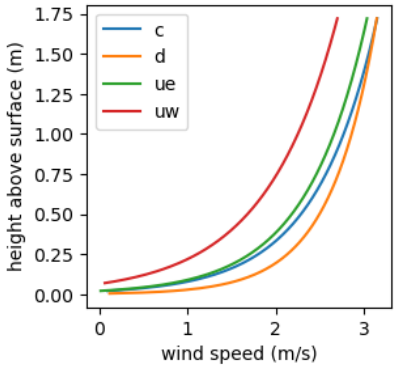


Figure 12. Meteorological conditions and the snow patch surface energy balance during the study period. (a) Dates of the snow-cover maps shown in Figure 11a, with fractional snow-covered area (fSCA). (b) Wind speed (line) and wind direction (points) measured by the eddy covariance system at 3 m on tower C. (c) Surface temperatures measured by infrared radiometers on towers C, D, UE and UW (solid lines), and air temperature at 3 m on tower C (dashed line). (d) Terms in the snow patch surface energy budget (Equation 7). We measured net radiation (R_{net}, blue line) (Section 3.3.2), vertical turbulent sensible heat flux over bare ground (H_u, red line), latent heat flux over bare ground (E_u, orange line) (Section 3.3.3), and snow melt energy (E_{melt}, black dots and bars). The blue line shows R_{net} calculated with the measured snow albedo of 0.56, and the blue band shows the minimum and maximum R_{net} for snow albedos between 0.45 and 0.6. We calculated E_{melt} from the melt of six snow patch transects (Figure 10); dots show the median, and bars show the minimum and maximum across all combinations of transects and snow densities. After 15 May, one patch melted out and the number of transects decreased from 6 to 3. We calculated Res (grey line) from the other energy fluxes (Equation 7); the grey band shows the minimum and maximum Res, combining the uncertainty in R_{net} and E_{melt}. Purple points show the mean modeled midday Q_H for $\epsilon = 0.4$; bars span from the lower quartile for $\epsilon = 0.6$ to the upper quartile for $\epsilon = 0.01$, combining variability across snow patches and wind profiles with uncertainty in the IBL height (Figure 11c). (e) Mean daily energy balance residual, Res (values printed above each bar).

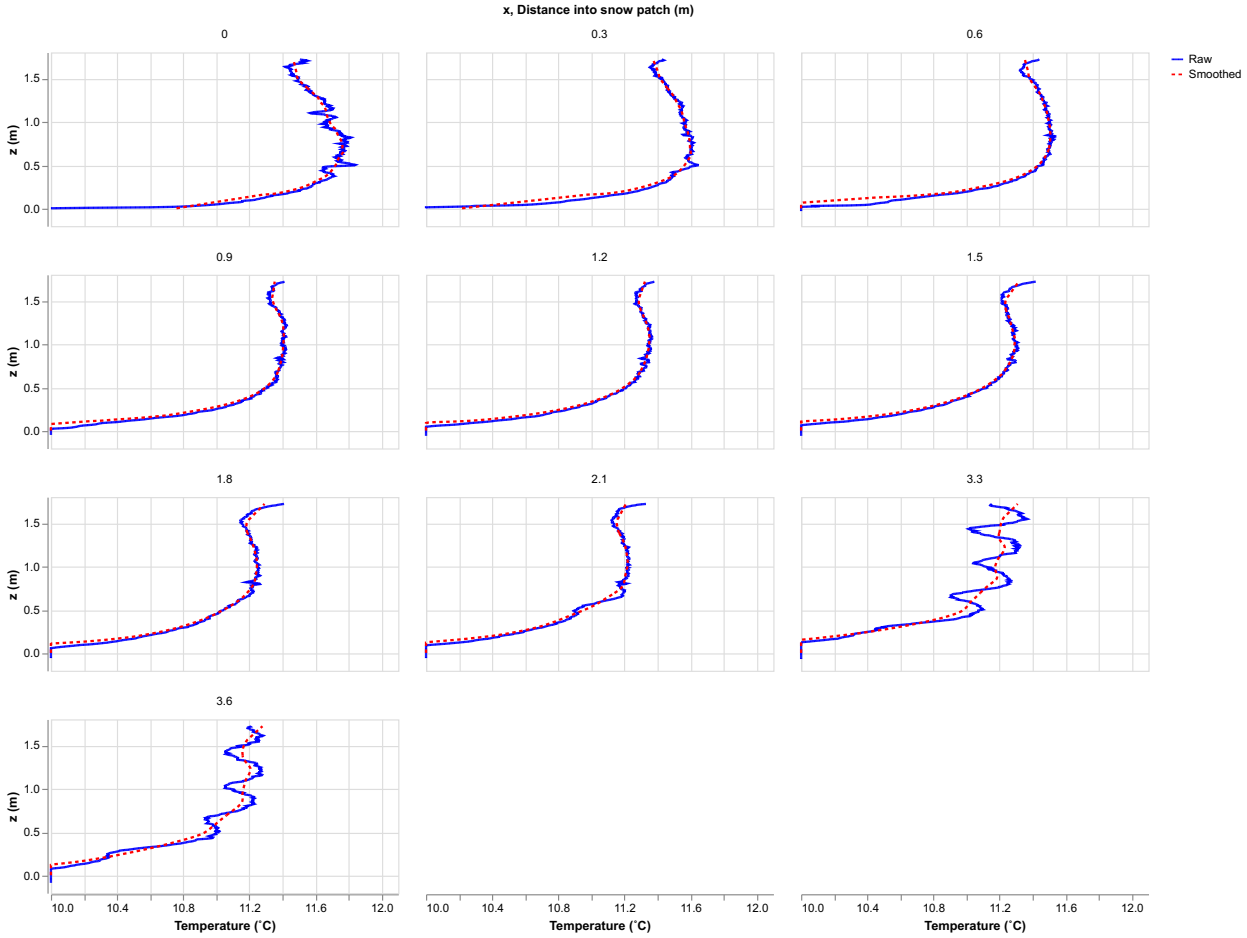
Supplemental Figures



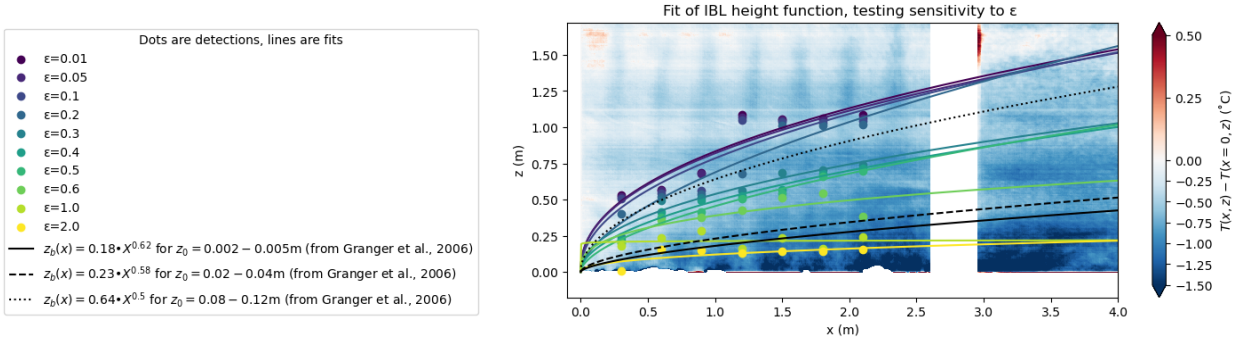
[Figure S1] Measurements and bulk estimates of sensible heat flux (Hu) and latent heat flux (Eu). Measurements are from eddy covariance sensors at 3 meters on the four towers. Bulk estimates use the COARE method (Cox et al., 2025) and use different 3-meter wind speeds inputs and surface temperatures measured on each of four towers. Surface humidity is assumed to be at saturation, although this only applies for snow cover. This results in unrealistically large latent heat fluxes once bareground is exposed.



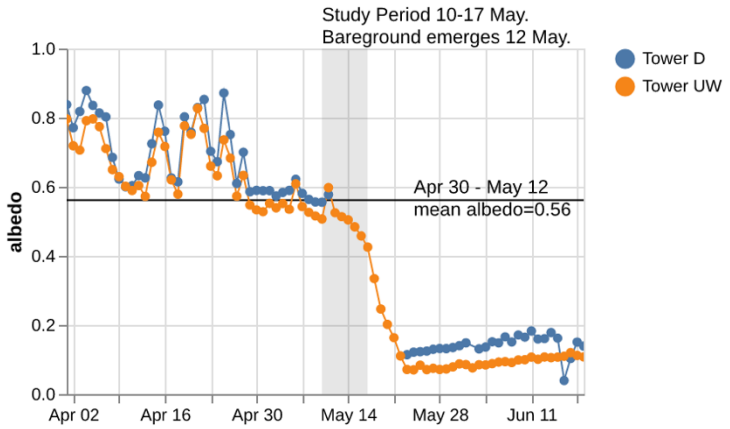
[Figure S2] Wind profiles calculated using 3-meter wind speed and shear velocity measurements from the four towers.



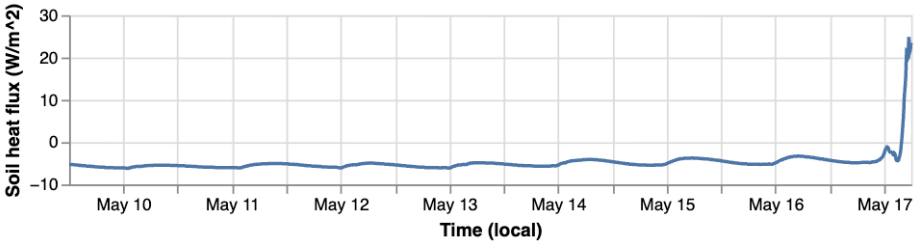
[Figure S3] Measured T(x,z) profiles extracted from the IR sheet (blue lines). Smoothed profiles (red dashed lines) are generated from a moving average over 5mm. Smoothed profiles are used to calculate vertical gradients in T(x,z).



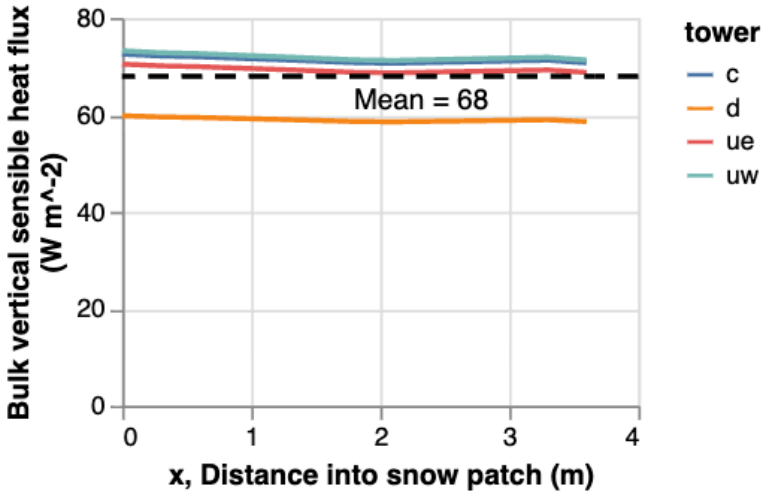
[Figure S4] Detected flux IBL heights (points) and fitted power-law curves for ten values of ε, overlaid on the temperature difference T(x, z) − T(x = 0, z). Fits use the first sheet only (x ≤ 2.1 m). Black lines show the temperature IBL growth curves of Granger et al. (2006, Eqs. 5a–5c) for three ranges of upwind roughness.



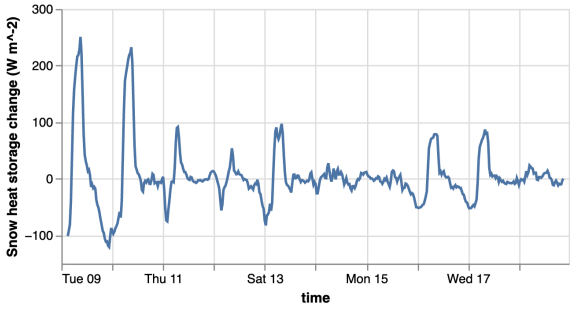
[Figure S5] Daily albedo estimates measured from upward and downward facing radiometers on towers (D and UW). Daily albedo was calculated using the 30-minute period with the highest incoming shortwave radiation.



[Figure S6] Direct measurements from ground heat flux from a soil heat flux plate near tower D.



[Figure S7] Vertical sensible heat flux over the snow patch calculated with the COARE method (Cox et al., 2025). Model inputs include wind speed and roughness lengths measured on the four towers, a snow surface temperature of 0˚C, mixing ratio measured at 1 m on tower C, and air temperature measurements measured at 1.5m on the IR sheet. The many measurements of air temperature at 1.5m on the IR sheet allow us to estimate bulk fluxes as a function of distance into the snow patch.



[Figure S8] Estimated snow heat storage change.

[Table S1] Estimates of Q_H. Mean Q_H is calculated for all Q_H estimated across the distribution of snow patch lengths on each day. We used 12 distinct models to estimate Q_H for snow patches; the 12 models are composed of four different estimates of z_0 from the four towers, and 3 different IBL heights.

		Date	2023-05-09	2023-05-10	2023-05-13	2023-05-15	2023-05-16	2023-05-23
IBL Fitting Method	Tower	z_0						
ε=0.01	d	0.0043	378	470	563	634	663	993
	c	0.0190	349	428	507	567	592	855
	ue	0.0212	333	409	483	540	563	810
	uw	0.0653	268	320	371	410	424	575
ε=0.4	d	0.0043	312	368	421	463	478	632
	c	0.0190	292	334	374	405	415	518
	ue	0.0212	280	319	355	384	394	489
	uw	0.0653	237	254	270	282	285	319
ε=0.6	d	0.0043	185	229	274	308	322	478
	c	0.0190	158	193	227	253	263	373
	ue	0.0212	150	182	214	238	248	349
	uw	0.0653	108	126	142	156	160	206

[Table S2] Fitted parameters and standard error of the model $Q_H(x) = \alpha x^{\beta}$, for the 12 models (see Figure 7).

		α	β	α standard error	β standard error
epsilon	**tower**				
ε=0.01	c	999.0	-0.35	44.0	0.053
	d	1169.0	-0.39	52.0	0.054
	ue	946.0	-0.35	42.0	0.053
	uw	661.0	-0.29	31.0	0.055
ε=0.4	c	578.0	-0.21	30.0	0.060
	d	721.0	-0.26	38.0	0.061
	ue	544.0	-0.20	28.0	0.060
	uw	338.0	-0.10	19.0	0.062
ε=0.6	c	434.0	-0.33	22.0	0.062
	d	562.0	-0.38	30.0	0.064
	ue	406.0	-0.33	21.0	0.061
	uw	232.0	-0.24	13.0	0.064